NANO LETTERS
Letter
pubs.acs.org/NanoLett

Tuning the Electronic Structure of Titanium Oxide Support to Enhance the Electrochemical Activity of Platinum Nanoparticles

Feifei Shi,[†,§] L. Robert Baker,[‡,§] Antoine Hervier,[‡,§] Gabor A. Somorjai,*[,‡,§] and Kyriakos Komvopoulos*[,†]

[†]Department of Mechanical Engineering and [‡]Department of Chemistry, University of California, Berkeley, California 94720, United States

[§]Materials Sciences Division, Lawrence Berkeley National Laboratory, Berkeley, California 94720, United States

S *Supporting Information*

ABSTRACT: Two times higher activity and three times higher stability in methanol oxidation reaction, a 0.12 V negative shift of the CO oxidation peak potential, and a 0.07 V positive shift of the oxygen reaction potential compared to Pt nanoparticles on pristine TiO_2 support were achieved by tuning the electronic structure of the titanium oxide support of Pt nanoparticle catalysts. This was accomplished by adding oxygen vacancies or doping with fluorine. Experimental trends are interpreted in the context of an electronic structure model, showing an improvement in electrochemical activity when the Fermi level of the support material in Pt/TiO_x systems is close to the Pt Fermi level and the redox potential of the reaction. The present approach provides guidance for the selection of the support material of Pt/TiO_x systems and may be applied to other metal-oxide support materials, thus having direct implications in the design and optimization of fuel cell catalyst supports.

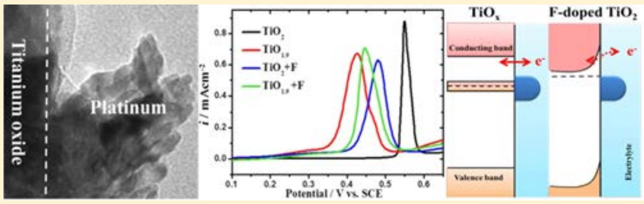

KEYWORDS: *Electronic structure, electrochemical activity, platinum nanoparticles, strong metal support interaction, titanium oxide*

Noble metal nanoparticles are widely used in heterogeneous catalysis. To satisfy different reaction requirements, the most commonly used technique is to fabricate bimetallic particles. An optimum electronic state can be achieved for certain reactions by adjusting the d-band energy of the bimetallic catalyst, for example, PtRu for methanol (CH_3OH) oxidation reaction (MOR) and PtCo for oxygen reduction reaction (ORR).[1−3] Recent research has shown that the catalytic behavior of metallic nanoparticles dispersed on a metal oxide support, which is usually inert by itself, can be significantly enhanced by the oxide support, a widely known phenomenon loosely referred to here as the strong metal support interaction (SMSI) effect.[4−10]

Metal oxides, TiO_2 in particular, have been used as supports of metal nanoparticles, such as Pt, Au, and Pd, because of their superior chemical stability under reducing and oxidizing conditions.[11−14] However, the use of these metal oxides as electrocatalysts is limited by their intrinsic low electrical conductivity.[15,16] It is therefore essential to design the structure of the catalyst so that to reduce undesirable side effects associated with the low electrical conductivity and poor interaction between the active Pt nanoparticles and the TiO_x support. Metallic or semiconducting behavior has been observed by reducing the metal oxide[17−19] or doping it with other metal cations.[16,20] While all of these approaches have shown that metal oxides are promising candidates for electrocatalyst supports, a systematic screening of potential semiconductor materials for electrochemical catalysis is still lacking.

Significantly enhanced electrocatalytic performance in important fuel cell reactions was achieved in this study via oxide support modification by either adding oxygen vacancies or doping with fluorine. Both of these methods adjust the electronic structure of the titanium oxide support, resulting in high electronic conductivity. Consequently, the MOR activity and stability increase by a factor of 1.75 and 2.7, respectively, relative to Pt nanoparticles on pristine TiO_2 support, the peak potential of CO oxidation is negatively shifted by 0.12 V, and the ORR potential is positively shifted by 0.07 V. An electronic structure model is developed by considering the combined effects of the support material Fermi level, the Pt Fermi level, and the redox potential of the reaction.

Two titanium oxide substrates with different stoichiometries (i.e., $TiO_{1.9}$ and TiO_2) were synthesized as previously described.[21−23] However, polished Ti plates were used in this study as the support material instead of a Si wafer. Thin films consisting of TiO_x were deposited by dc magnetron sputtering. The oxygen vacancy concentration of the highly oxygen deficient sputtered films was tuned by rapid thermal annealing in O_2 at various temperatures. All of the samples were first annealed in N_2 to minimize variation in grain size. Stoichiometric ratios were determined from the Ti^{3+}-to-Ti^{4+} ratio obtained from the Ti 2p X-ray photoelectron spectroscopy (XPS) spectra (see Figure S1, Supporting Information). Fluorine doping was accomplished by plasma treatment in N_2

Received: June 29, 2013
Revised: August 4, 2013
Published: August 7, 2013

gas and trace amounts of sulfur hexafluoride (SF_6). This treatment yielded two fluorine-doped TiO_x surfaces (designated as $TiO_{1.9}$ + F and TiO_2 + F) with different amounts of O vacancies.

Platinum films were electroplated using 0.5 M chloroplatinic acid (H_2PtCl_6) as the precursor and 0.1 M KCl as the support electrolyte. Electroplating was accomplished by performing 10 cycles of potential scan between −0.1 and −0.9 V versus SCE (saturated calomel electrode) at a rate of 50 mV/s using differently treated TiO_x substrates. Loading of Pt was controlled by the number of scan cycles. The lower and upper bound of cyclic voltammetry affected the size and dispersion of the Pt nanoparticles.[24] The same electroplating conditions were used for all substrate materials.

The surface morphology of the Pt nanoparticles was examined with a scanning electron microscope (SEM, JEOL, JSM-6700F). The structure and size distribution of the nanoparticles were measured with a transmission electron microscope (TEM, JEOL, JEM-3000F). TEM samples were prepared by removing the Pt film from the Ti substrate with a pair of dissecting forceps in the presence of a small amount of ethanol and then placing the Pt film onto a copper grid and drying in air at room temperature.

Electrochemical measurements were obtained with a CHI 660D electrochemistry workstation connected to a three-electrode cell system (see Figure S2, Supporting Information). The working electrode consisted of a thin Pt film deposited on a TiO_x substrate and was vertically placed in the cell, while the counter and reference electrodes consisted of Au foil and Ag/AgCl, respectively. However, all reported potentials are referred to a SCE or a normal hydrogen electrode (NHE) (only for ORR and hydrogen evolution reaction (HER)). To avoid different surface resistance effects, *iR*-compensation correction was used in all electrochemical experiments. The electrolyte consisted of deaerated (by purging high-purity N_2 gas) 0.5 M H_2SO_4 with or without 0.5 M CH_3OH, 0.5 M H_2SO_4 saturated with CO, or 0.5 M H_2SO_4 saturated with O_2. High-purity chemicals, gases, and H_2O (∼18 MΩ) were used in all electrochemical experiments performed at room temperature (25 ± 1 °C).

Figure 1a shows a plane-view SEM image of as-prepared Pt nanoparticles deposited on a $TiO_{1.9}$ substrate. The nanoparticles demonstrate cluster-like morphology of relatively uniform size distribution (15−20 nm) and good dispersion on the substrate surface. Figure 1b shows a bright-field TEM image of the Pt nanoparticles (dark) deposited on the $TiO_{1.9}$ substrate. The lattice fringe of the Pt(111) plane (2.3 Å) measured from the high-resolution TEM (HRTEM) image shown in Figure 1c and the TiO_2 anatase (101) plane (3.5 Å) indexed in Figure 1b indicate the formation of polycrystalline Pt nanoparticle clusters on the $TiO_{1.9}$ substrate. These TEM images reveal that Pt nanoparticles of ∼5 nm average size clustered and adhered to the $TiO_{1.9}$ substrate, producing a polycrystalline Pt structure. Since differences in the morphology and polycrystalline structure of the Pt nanoparticles were not observed with other samples, SEM and TEM images of these nanoparticles are not shown here. In view of the similar morphology and polycrystalline structure of the Pt nanoparticles synthesized on different TiO_x substrates under the same conditions, differences in the electrochemical performance of different samples (discussed below) are attributed to the SMSI effect.

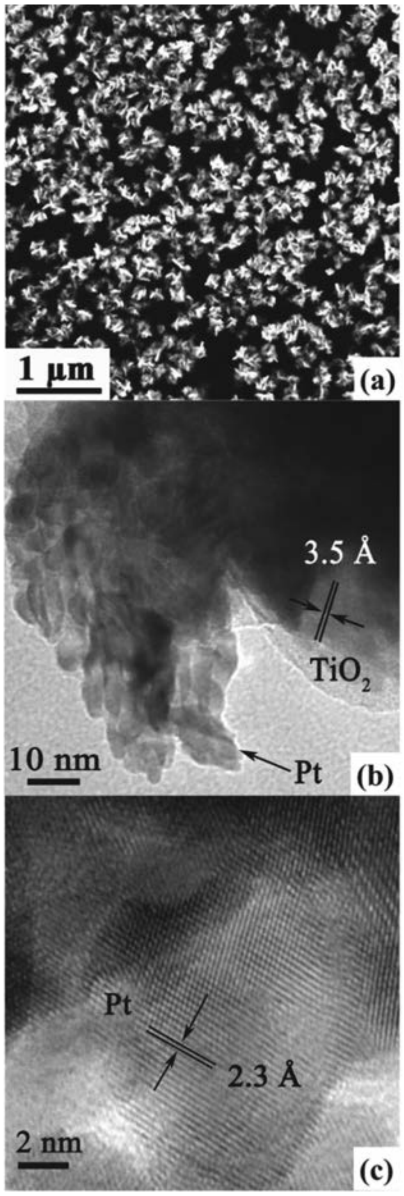

Figure 1. (a) SEM and (b,c) TEM images of Pt nanoparticles on a $TiO_{1.9}$ substrate.

The electrochemically active Pt surface area was characterized by cyclic voltammetry (CV) experiments performed at room temperature with different Pt/TiO_x and Pt/TiO_x + F electrodes in a sulfuric acid (0.5 M H_2SO_4) solution (Figure 2a). The electrodes were cycled between −0.2 and 1.2 V at a scan rate of 50 mV/s, while the electrolyte was continuously purged with Ar. A CV curve typical of polycrystalline Pt in the H-adsorption/desorption region and a similar double-layer capacitance were obtained with all Pt/TiO_x electrodes. To normalize the activity in other reactions, the Pt surface area of different substrates was determined by integrating the H-adsorption/desorption interval, subtracting the double-layer charging current, and dividing the resulting Coulomb charge by 2 and 210 $\mu C/cm^2$ (the charge to remove a monolayer of hydrogen from a platinum surface[25]). The roughness factor of different Pt/TiO_x catalysts, defined as the ratio of the electrochemically active area (ECA) to the nominal electrode area,[26] is given in Table 1. The similar roughness factor of the Pt catalyst on different TiO_x substrates is due to the similar

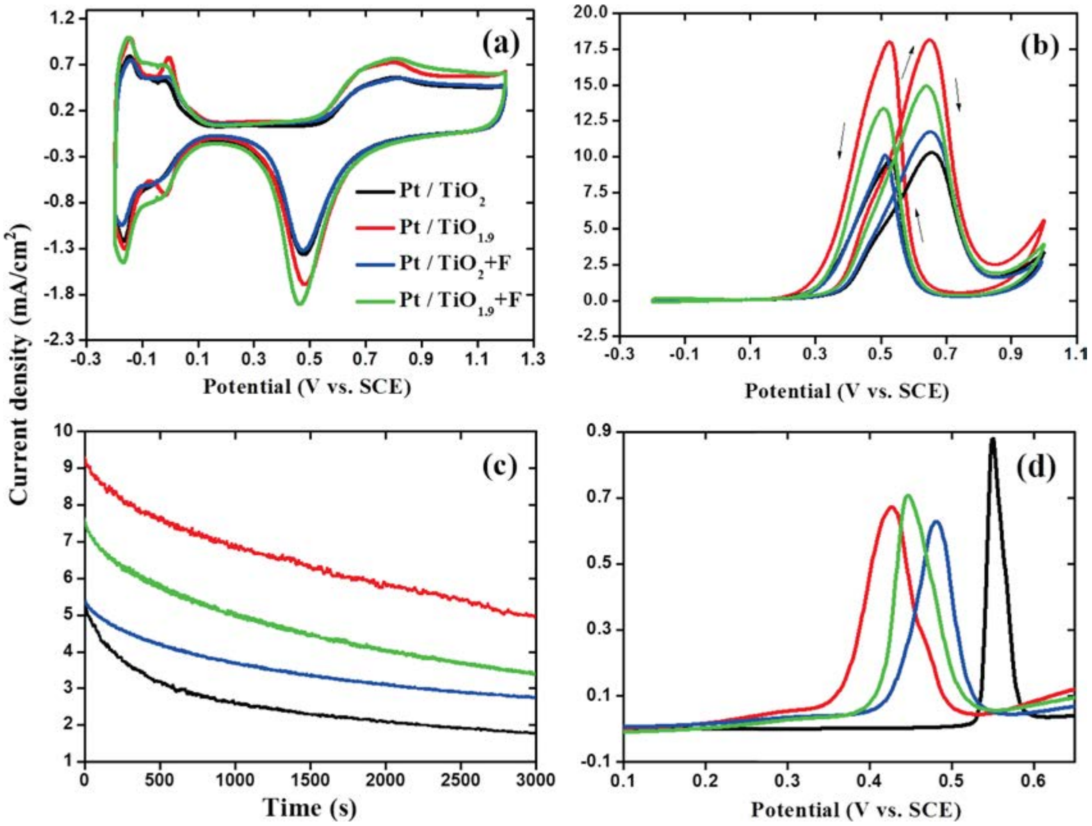

Figure 2. Cyclic voltammograms for (a) 0.5 M H_2SO_4 solution (scan rate = 50 mV/s) and (b) 0.5 M CH_3OH and 0.5 M H_2SO_4 solution (scan rate = 20 mV/s), (c) current versus time measured at 0.5 V vs SCE for 0.5 M CH_3OH and 0.5 M H_2SO_4 solution, and (d) CO stripping voltammograms for 0.5 M H_2SO_4 solution (scan rate = 10 mV/s). (Arrows indicating upward and downward scanning are only shown for the Pt/$TiO_{1.9}$ electrode for clarity.).

Table 1. Electrochemical Characterization of Pt Nanoparticles on Different TiO_x Supports

		current density (mA/cm^2)		potential (V vs SCE)	
system	roughness factor(a) (cm^2/cm^2)	i_{p}(b)	i_{3000}(c)	U_{MOR}(d)	U_{CO}(e)
Pt/$TiO_{1.9}$	13.3	1.40	0.38	0.64	0.43
Pt/$TiO_{1.9}$+F	14.1	1.10	0.24	0.64	0.45
Pt/TiO_2+F	12.9	0.97	0.23	0.65	0.48
Pt/TiO_2	12.1	0.80	0.14	0.66	0.55
Pt foil	3.1	0.48	0.05	0.65	0.70

(a)Specific mass area measured from the evolution of the hydrogen area. (b)Normalized peak current density of the positive scan measured in 0.5 M CH_3OH and 0.5 M H_2SO_4 (scan rate = 20 mV/s). (c)Normalized current density measured by chronoamperometry after 3000 s at 0.5 V (vs SCE). (d)Peak position of methanol oxidation reaction in positive scan measured in 0.5 M CH_3OH and 0.5 M H_2SO_4 (scan rate = 20 mV/s). (e)Peak position of CO stripping (scan rate = 10 mV/s).

loading and structure of the Pt nanoparticles, as shown by SEM and TEM results (Figure 1). The significantly higher ECA of the Pt/TiO_x and Pt/TiO_x + F catalysts than the typical two-dimensional Pt catalyst (Pt foil) may be attributed to the small size and good dispersion of the Pt nanoparticles. The absence of any other oxidation or reduction peak in the CV curves shown in Figure 2a indicates that the TiO_x and TiO_x + F substrates are electrochemically stable in acidic solutions and oxidative environments.[16,20,27]

MOR CV curves obtained at room temperature with Pt/TiO_x and Pt/TiO_x + F electrodes in an aqueous solution of 0.5 M CH_3OH and 0.5 M H_2SO_4 revealed a much higher current density for the Pt/$TiO_{1.9}$ electrode than all other electrodes (Figure 2b). The CH_3OH electro-oxidation positive-scan peak of the Pt/$TiO_{1.9}$ electrode is at ~0.64 V and the onset potential (defined as the potential corresponding to a 0.1 mA/cm^2 current density) is equal to 0.28 V. In the case of the Pt/$TiO_{1.9}$ + F, Pt/TiO_2, and Pt/TiO_2 + F electrodes, the anodic peak potential is observed at 0.64, 0.66, and 0.65 V and the corresponding onset potential is equal to 0.35, 0.42, and 0.41 V, respectively. Considering the significance of a lower onset potential and a higher peak current density in MOR, the $TiO_{1.9}$ substrate with oxygen vacancies shows the best electrochemical performance, while the TiO_2 + F substrate is ranked third among all samples. However, both treatments enhance the catalytic performance compared to the Pt/TiO_2 electrode.

Chronoamperograms of the electroactivity of the four electrodes in a 0.5 M CH_3OH and 0.5 M H_2SO_4 aqueous solution obtained at room temperature with an oxidation potential of 0.5 V (vs SCE) shows a gradual decrease in MOR electroactivity with increasing time and a strong dependence of the rate of current density decrease on the type of TiO_x substrate (Figure 2c). The Pt/$TiO_{1.9}$ electrode shows the least decrease in current density, while the electron density corresponding to the Pt/TiO_2 electrode shows a decrease by 50% within 1000 s. The higher current density of the Pt/$TiO_{1.9}$ electrode may be attributed to the increased CO tolerance, that is, CO can be effectively oxidized and removed from the surface of the Pt nanoparticles.

Voltammetry experiments of preadsorbed CO were performed with a 0.5 M H_2SO_4 electrolyte (purged with N_2 gas for 30 min at 0 V after CO adsorption) using a scan rate of 10 mV/s. The CO stripping voltammograms indicate that the Pt/$TiO_{1.9}$ electrode exhibits the highest CO tolerance. The Pt/$TiO_{1.9}$ peak potential (0.43 V vs SCE) shows a negative shift of 0.12 V relative to Pt/TiO_2 (0.55 V vs SCE). Because the same electrodeposition method was used to prepare all Pt nanoparticle catalysts and differences between the catalysts were not visible by SEM and TEM, implying no influence of other factors (e.g., Pt nanoparticle size or treatment conditions) on the CO oxidation peak,[28−30] peak shifting is attributed to the SMSI effect. Detailed information about the roughness factor, peak current density i_p, current density after 3000 s of testing i_{3000}, MOR peak potential U_{MOR}, and peak potential of CO striping U_{CO} for the four electrodes examined and pure Pt foil are given in Table 1. Since CO is an important intermediate product, its oxidation capability significantly influences the MOR activity. With CO more effectively oxidized and removed from the Pt surface, better electrocatalysis performance is achieved, which is in good agreement with the finding that both i_p and i_{3000} increase with the decrease of U_{CO}. The results shown in Figure 2 and Table 1 indicate an enhancement of the catalytic performance (i.e., activity, stability, and toxic tolerance) in electrode order Pt < Pt/TiO_2 < Pt/TiO_2 + F < Pt/$TiO_{1.9}$ + F < Pt/$TiO_{1.9}$.

The substrate effect in small-molecule oxidation reactions of Pt catalysts and trend in catalyst performance demonstrated by the results shown in Figure 2 and Table 1 raise a question about whether a similar substrate effect and trends exist in reduction reactions, such as HER and ORR. To examine this prospect, HER and ORR polarization curves were obtained with different Pt/TiO_x electrodes in a N_2- or O_2-saturated aqueous solution of 0.5 M H_2SO_4 using a scan rate of 10 mV/s and stationary electrodes oriented vertically. The HER current−potential response shows a weak correlation with the substrate material (Figure 3a). The absence of a substrate effect is attributed to the fast kinetics under room-temperature reaction conditions.[28] However, the ORR polarization curves show a higher onset potential for Pt/$TiO_{1.9}$ and Pt/$TiO_{1.9}$ + F electrodes compared to Pt/TiO_2 + F and Pt/TiO_2 electrodes (Figure 3b). On the basis of the onset potential, the electrode performance under ORR conditions is ranked as Pt/TiO_2 < Pt/TiO_2 + F < Pt/$TiO_{1.9}$ + F < Pt/$TiO_{1.9}$, which is the same with the ranking of small-molecule oxidation reactions, that is, MOR and CO oxidation.

The SMSI effect observed in this study can be explained by a model of the charge transfer mechanism in nonstoichiometric $TiO_{1.9}$ and F-doped stoichiometric TiO_2 (Figure 4). TiO_2 has a band gap of 3.2 eV, while the work function of polycrystalline Pt is about 5.6−5.8 eV.[31] Oxygen vacancies introduced in the lattice of TiO_2 produce energy levels in the band gap (midgap states) about 0.5−1.0 eV below the conduction band E_c.[32] Because midgap states do not exist in stoichiometric TiO_2, fluorine acts as n-type dopant, producing donor states just below the conduction band (by $\sim k_BT$). The electronic structures of the substrate materials used in this study have been characterized in previous studies.[21−23] Both oxygen vacancies and fluorine doping generate a population of surface electrons available for conduction. In the case of F-doped titanium suboxide (TiO_x, $x < 2$), the primary effect of F is to passivate oxygen-vacancy defect states. However, because F doping can never fully passivate this sub-band, the remaining O vacancy states pin the Fermi level E_F. As a result, F doping produces an opposite effect in stoichiometric TiO_2 than reduced TiO_x. This contrasting effect of F-doping is reflected in the observed electrode performance trend, that is, Pt/TiO_2 < Pt/TiO_2 + F < Pt/$TiO_{1.9}$ + F < Pt/$TiO_{1.9}$.

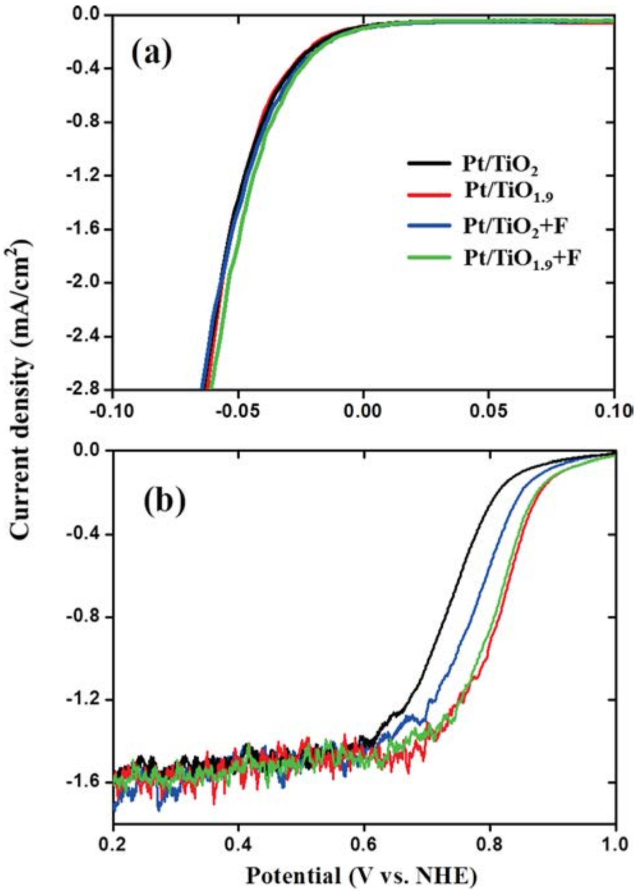

Figure 3. Polarization curves of (a) hydrogen current in N_2-saturated electrolyte and (b) ORR current in O_2-saturated electrolyte for different catalyst systems. The current was normalized by the apparent area (0.1964 cm^2) of the electrode. (scan rate = 10 mV/s, electrolyte = 0.5 M H_2SO_4).

The charge transfer capability of a semiconductor electrode depends on the existence of an energy barrier. In the absence of an energy barrier, the behavior of a semiconductor electrode is similar to that of a metallic electrode because most of the charge carriers are available for charge transfer. However, in the presence of an energy barrier, only a few charge carriers are available for charge transfer, and reactions induced by electron transfer are relatively slow.[33−35] For nonstoichiometric TiO_x, the midgap states yield a relatively low Fermi level (5.0−5.5 eV), assisting in electron transfer among the electrode, the Pt catalyst (5.6−5.8 eV), and the electrolyte (4.44−5.67 eV) (Figure 4a). In contrast, because F-doped TiO_2 has a higher Fermi level (~4.5 eV) than TiO_x ($x < 2$), an energy barrier (i.e., band bending) is produced to maintain equilibrium, which inhibits electron transfer and, in turn, reaction (Figure 4b). This explains the higher reactivity of $TiO_{1.9}$ than TiO_2 + F in the lower redox potential reactions, that is, MOR, ORR, and CO oxidation. However, for reactions with a high redox

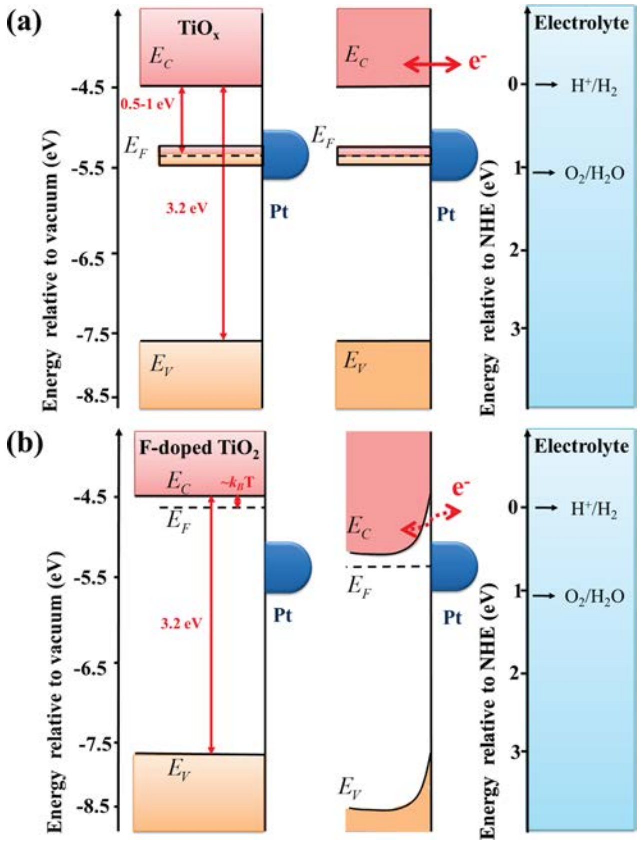

Figure 4. Schematic of charge transfer mechanism in (a) nonstoichiometric TiO$_x$ and (b) F-doped stoichiometric TiO$_2$. Midgap states in TiO$_x$ produce a relatively low Fermi level, assisting in electron transfer from the oxide to the adsorbed species. However, in the case of F-doped TiO$_2$, an energy barrier (band bending) is produced to maintain equilibrium, which inhibits electron transfer and, in turn, chemical reaction. (E_C, E_F, and E_V denote conduction, Fermi, and valence energy levels, respectively.).

potential, such as HER (~4.44 eV, pH = 1),[15] all substrate materials exhibit a similar effect.

Two different methods, that is, addition of oxygen vacancies and fluorine doping, were used in this study to modify the electronic structure of the titanium oxide support of Pt nanoparticle catalysts and systematically evaluate the resulting electrochemical activity. Among the reactions studied, only HER is support insensitive, while MOR shows an increase in activity and stability by a factor of 1.75 and 2.7, respectively, the CO oxidation peak exhibits a negative shift by 0.12 V, implying better antipoisoning capability, and the ORR potential shows a positive shift by 0.07 V compared to Pt nanoparticles on pristine TiO$_2$ support. To explain the observed trends, an electronic structure model of Pt/TiO$_x$ electrocatalyst systems was introduced that shows an enhancement of the electrochemical activity of the Pt nanoparticles when the Fermi level of the support material is close to the Pt Fermi level and the redox potential of the reaction so that to facilitate electron transfer among the electrode, the Pt nanoparticles, and the electrolyte. The present approach provides guidance for the selection of the support material of Pt/TiO$_x$ systems and can also be applied to other metal-oxide support materials, facilitating the design and optimization of new support materials of fuel cell catalysts.

■ ASSOCIATED CONTENT

Ⓢ Supporting Information

Additional information and figures. This material is available free of charge via the Internet at http://pubs.acs.org.

■ AUTHOR INFORMATION

Corresponding Author

*(G.A.S.) Tel.: 510-642-4053. Fax: 510-643-9668. E-mail: somorjai@berkeley.edu. (K.K.) Tel.: (510) 642-2563. Fax: (510) 642-5539. E-mail: kyriakos@me.berkeley.edu.

Notes

The authors declare no competing financial interest.

■ ACKNOWLEDGMENTS

The authors thank Dr. Philip N. Ross, Jr., for helpful discussions on elertocatalysis, Zhongwei Zhu for assistance in XPS spectra acquisition, and Yimin Li and Hailiang Wang for fruitful discussions. TiO$_x$ film deposition was carried out at the Marvell Nano Lab, University of California, Berkeley (UCB). SEM and XPS studies were carried out at the Molecular Foundry, Lawrence Berkeley National Laboratory. This research was supported by the UCB−KAUST Academic Excellence Alliance (AEA) Program.

■ REFERENCES

(1) Stamenkovic, V.; Mun, B. S.; Mayrhofer, K. J. J.; Ross, P. N.; Markovic, N. M.; Rossmeisl, J.; Greeley, J.; Norskov, J. K. *Angew. Chem. Int. Ed.* **2006**, *45*, 2897−2901.

(2) Wang, C.; Chi, M.; Li, D.; Strmcnik, D.; van der Vliet, D.; Wang, G.; Komanicky, V.; Chang, K.-C.; Paulikas, A. P.; Tripkovic, D.; Pearson, J.; More, K. L.; Markovic, N. M.; Stamenkovic, V. R. *J. Am. Chem. Soc.* **2011**, *133*, 14396−14403.

(3) Watanabe, M.; Motoo, S. *Electroanal. Chem. Interfacial Electrochem.* **1975**, *60*, 267−273.

(4) Schwab, G.-M. *Discuss. Faraday Soc.* **1950**, *8*, 166−171.

(5) Tauster, S. J.; Fung, S. C.; Garten, R. L. *J. Am. Chem. Soc.* **1978**, *100*, 170−175.

(6) Kowal, A.; Li, M.; Shao, M.; Sasaki, K.; Vukmirovic, M. B.; Zhang, J.; Marinkovic, N. S.; Liu, P.; Frenkel, A. I.; Adzic, R. R. *Nat. Mater.* **2009**, *8*, 325−330.

(7) Masa, J.; Bordoloi, A.; Muhler, M.; Schuhmann, W.; Xia, W. *Chem. Sus. Chem.* **2012**, *5*, 523−525.

(8) Hayden, B. E.; Malevich, D. V.; Pletcher, D. *Electrochem. Commun.* **2001**, *3*, 395−399.

(9) He, X.; Hu, C. *J. Power Sources* **2011**, *196*, 3119−3123.

(10) Sun, Z.; Wang, X.; Liu, Z.; Zhang, H.; Yu, P.; Mao, L. *Langmuir* **2010**, *26*, 12383−12389.

(11) Yoo, S. J.; Jeon, T.-Y.; Lee, K.-S.; Park, K.-W.; Sung, Y.-E. *Chem. Commun.* **2010**, *46*, 794−796.

(12) Chu, Y.-Y.; Wang, Z.-B.; Jiang, Z.-Z.; Gu, D.-M.; Yin, G.-P. *Adv. Mater.* **2011**, *23*, 3100−3104.

(13) Murdoch, M.; Waterhouse, G. I. N.; Nadeem, M. A.; Metson, J. B.; Keane, M. A.; Howe, R. F.; Llorca, J.; Idriss, H. *Nat. Chem.* **2011**, *3*, 489−492.

(14) Abida, B.; Chirchi, L.; Baranton, S.; Napporn, T. W.; Kochkar, H.; Léger, J.-M.; Ghorbel, A. *Appl. Catal. B: Environ.* **2011**, *106*, 609−615.

(15) Grätzel, M. *Nature* **2001**, *414*, 338−344.

(16) Subban, C. V.; Zhou, Q.; Hu, A.; Moylan, T. E.; Wagner, F. T.; DiSalvo, F. J. *J. Am. Chem. Soc.* **2010**, *132*, 17531−17536.

(17) Inglis, A. D.; Le Page, Y.; Strobel, P.; Hurd, C. M. *J. Phys. C: Solid State Phys.* **1983**, *16*, 317−333.

(18) Ioroi, T.; Senoh, H.; Yamazaki, S.; Siroma, Z.; Fujiwara, N.; Yasuda, K. *J. Electrochem. Soc.* **2008**, *155*, B321−B326.

(19) Ioroi, T.; Siroma, Z.; Fujiwara, N.; Yamazaki, S.; Yasuda, K. *Electrochem. Commun.* **2005**, *7*, 183−188.

(20) Ho, V. T. T.; Pan, C.-J.; Rick, J.; Su, W.-N.; Hwang, B.-J. *J. Am. Chem. Soc.* **2011**, *133*, 11716−11724.

(21) Baker, L. R.; Hervier, A.; Seo, H.; Kennedy, G.; Komvopoulos, K.; Somorjai, G. A. *J. Phys. Chem. C* **2011**, *115*, 16006−16011.

(22) Seo, H.; Baker, L. R.; Hervier, A.; Kim, J.; Whitten, J. L.; Somorjai, G. A. *Nano Lett.* **2011**, *11*, 751−756.

(23) Hervier, A.; Baker, L. R.; Komvopoulos, K.; Somorjai, G. A. *J. Phys. Chem. C* **2011**, *115*, 22960−22964.

(24) Tian, N.; Zhou, Z.-Y.; Sun, S.-G.; Ding, Y.; Wang, Z. L. *Science* **2007**, *316*, 732−735.

(25) Schmidt, T. J.; Gasteiger, H. A.; Stäb, G. D.; Urban, P. M.; Kolb, D. M.; Behm, R. J. *J. Electrochem. Soc.* **1998**, *145*, 2354−2358.

(26) Bard, A. J.; Faulkner, L. R. *Electrochemical Methods: Fundamentals and Applications*; Wiley: New York, 2001.

(27) Pourbaix, M. *Atlas of Electrochemical Equilibria in Aqueous Solution*, 2nd ed.; National Association of Corrosion Engineers: Houston, TX, 1974.

(28) Marković, N. M.; Ross, P. N., Jr. *Surf. Sci. Rep.* **2002**, *45*, 117−229.

(29) Arenz, M.; Mayrhofer, K. J. J.; Stamenkovic, V.; Blizanac, B. B.; Tomoyuki, T.; Ross, P. N.; Markovic, N. M. *J. Am. Chem. Soc.* **2005**, *127*, 6819−6829.

(30) Hayden, B. E.; Pletcher, D.; Suchsland, J.-P.; Williams, L. J. *Phys. Chem. Chem. Phys.* **2009**, *11*, 9141−9148.

(31) Wilson, R. G. *J. Appl. Phys.* **1966**, *37*, 2261−2267.

(32) Cronemeyer, D. C. *Phys. Rev.* **1959**, *113*, 1222−1226.

(33) Bott, A. W. *Curr. Sep.* **2001**, *19*, 71−75.

(34) Zhang, Z.; Yates, J. T., Jr. *Chem. Rev.* **2012**, *112*, 5520−5551.

(35) Linsebigler, A. L.; Lu, G.; Yates, J. T., Jr. *Chem. Rev.* **1995**, *95*, 735−758.